Tunable-Generalization Diffusion Powered by Self-Supervised Contextual Sub-Data for Low-Dose CT Reconstruction

Guoquan Wei, Zekun Zhou, Liu Shi, Wenzhe Shan, Qiegen Liu, *Senior Member, IEEE*

***Abstract*— Current models based on deep learning for low-dose CT denoising rely heavily on paired data and generalize poorly. Even the more concerned diffusion models need to learn the distribution of clean data for reconstruction, which is difficult to satisfy in medical clinical applications. At the same time, self-supervised-based methods face the challenge of significant degradation of generalizability of models pre-trained for the current dose to expand to other doses. To address these issues, this paper proposes a novel method of tunable-generalization diffusion powered by self-supervised contextual sub-data for low-dose CT reconstruction, named SuperDiff. Firstly, a contextual subdata similarity adaptive sensing strategy is designed for denoising centered on the LDCT projection domain, which provides an initial prior for the subsequent progress. Subsequently, the initial prior is used to combine knowledge distillation with a deep combination of latent diffusion models for optimizing image details. The pre-trained model is used for inference reconstruction, and the pixel-level self-correcting fusion technique is proposed for fine-grained reconstruction of the image domain to enhance the image fidelity, using the initial prior and the LDCT image as a guide. In addition, the technique is flexibly applied to the generalization of upper and lower doses or even unseen doses. Dual-domain strategy cascade for self-supervised LDCT denoising, SuperDiff requires only LDCT projection domain data for training and testing. Full qualitative and quantitative evaluations on both datasets and real data show that SuperDiff consistently outperforms existing state-of-the-art methods in terms of reconstruction and generalization performance.**

***Index Terms*— Low-dose CT reconstruction, self-supervised, diffusion model, tunable generalization.**

I. Introduction

COMPUTED tomography (CT) is a widely used medical imaging technique in clinical scenarios, but the radiation exposure inherent in CT may increase the risk of radiologic cancers [1], [2]. In contrast, low-dose CT (LDCT) mitigates this risk by reducing the radiation dose to the patient by lowering the tube current. However, this can result in significant noise and artifacts in the reconstructed CT image, ultimately compromising diagnostic performance [3].

Over the past few decades, LDCT reconstruction has produced numerous commendable results that have contributed greatly to improving the quality of LDCT. These studies fall into three main categories: 1) sinusoidal domain data filtering [4], 2) iterative reconstruction [5]– [7], and 3) image post-processing techniques [8], [9]. Sinusoidal domain filtering, such as bilateral filtering method [10], penalized weighted least squares (PWLS) [11], anisotropic filtering [12], [13], etc., operates directly on the projected domain data. However the filtering process may lead to loss of frequency domain information and reduce the spatial resolution of the image. Iterative reconstruction, which requires a design that incorporates system information, noise assumptions, and image a priori information as prerequisites, and often requires the iterative execution of forward and backward projections. The time cost and process complexity define the upper limit of its clinical application. Image post-processing techniques are applied to the reconstructed LDCT images to enhance the image quality, such as block matching based 3D filtering (BM3D) [14], which filters and integrates the 3D combinations obtained from similar matching to obtain denoising results, and demonstrates excellent performance in LDCT imaging.

In recent years, deep learning (DL) in medical imaging shows potential for more clinical applications than traditional methods [15], [16]. Currently, DL-based CT reconstruction is mainly based on data-driven optimization of multi-level neural networks, and after obtaining the optimal solution, the model is used to predict the denoised images. However, current deep learning based methods either use supervised methods that rely on paired data [17]– [20] or self-supervised methods with paired noise [21], self-supervised learning with batch data similarity [22] or unsupervised learning with real data using diffusion models [23]– [25]. In the CT denoising task, the supervised need for paired data is difficult to satisfy under clinical circumstances, and we cannot implement different scanning modalities for the same patient to obtain paired and aligned data. Even though we can simulate the construction of paired data, the actual noise generation is often affected by the instrument settings, the operation process, and the object being scanned, and cannot be fully equated to the real LDCT, which is why supervised learning generalizes poorly and unsupervised methods usually use clean images as the starting point for analysis. On the contrary, self-supervised

This work was supported by the National Natural Science Foundation of China (621220033, 62201193). (G. Wei is the first author.) (Co-corresponding authors: L. Shi and Q. Liu.)

G. Wei, L. Shi, W. Shan, and Q. Liu are with the School of Information Engineering, Z. Zhou is with School of Mathematics and Computer Sciences, Nanchang University, Nanchang 330031, China (email:{shiliu, shan, liuqiegen}@ncu.edu.cn, {guoquanwei, zekunzhou}@email.ncu.edu.cn).

methods do not require the involvement of clean data, but only noise-containing images, and are a well-suited method for application in clinical LDCT denoising tasks. However, current self-supervised methods still need to address the problem of poor reconstruction of untrained doses.

Diffusion modeling (DM) [26] has recently emerged as a novel and influential explicit generative model that has been widely used in medical image reconstruction with impressive results. Its forward diffusion process is a stationary Markov chain that gradually introduces Gaussian noise according to the noise scheduling until it is converted to a completely random standard Gaussian noise. The inverse process, on the other hand, utilizes a denoising network to predict the noise, converting the standard Gaussian samples into specific image samples from the target distribution based on the Markov chain. Although DM has been shown to achieve high-quality reconstruction [27], the standard diffusion model still suffers from 1) long sampling time of 1000 steps, difficult to train with high resolution, and difficulty in lightweight deployment. All these pose challenges to the clinical application of LDCT denoising [28]. 2) In the absence of real data distribution involved, the results are usually not good. For this reason, a series of methods such as accelerated samplers [29], [30], domain iterative diffusion [31], latent diffusion [32], [33], and guided diffusion [34], [35] have emerged.

In order to fit the clinical application, the aim of this paper is to explore a low-dose denoising method that relies only on a single noise projection domain and does not rely on the distribution of real data for modeling. To this end, this study proposes tunable-generalization diffusion powered by self-supervised contextual sub-data for low-dose CT reconstruction. A contextual LDCT projection domain self-enhancing similarity strategy is designed to adequately remove the noise under the data domain, which can enhance the fidelity and mitigate the smoothness. The results are further optimized in the image domain considering the complexity of noise and incomplete detail recovery. For this purpose, the initial prior is used to deeply combine the knowledge distillation technique with the latent diffusion model to perceive the data consistency and refinement. In the inference stage, the initial prior and LDCT images are introduced as a guide to fully utilize the model effectiveness as well as the matching training process. On this basis, a pixel-level self-correcting fusion is proposed to balance the differences between the bootstrap information, and the technique is skillfully applied to the generalization of the upper and lower doses as well as the dose of unseen data. This study emphasizes that SuperDiff requires only LDCT projection domain data, and the reconstruction effect and generalization are greatly improved.

In summary, the work of this paper can be described as:

- A novel self-supervised denoising model SuperDiff starting from a single sheet of noisy projection data is proposed. A self-enhancing similarity strategy for contextual projection sub-data is designed for sufficiently removing the nonlinear noise under the projection domain to provide an effective initial prior.
- Knowledge distillation is deeply combined with latent diffusion model. Mapping the image domain to the latent space, with the help of Gaussian diffusion mechanism and transformer denoising network to fully perceive the details and enhance the reconstruction effect.
- SuperDiff uses the projection domain prior and the LDCT image as a guide in the inference phase, and the pixel-level self-correcting fusion technique improves the balance between the two, facilitating data fidelity and lesion reproduction. The technique is also used for tunable generalization of up and down dose, unseen dose and real clinical data.

II. Related Work

A. Denoising Research under Statistical Theory

Given a LDCT projection measure y_{ld}, the inverse problem is to recover to clean data y_0. Its corresponding image domain can be described as:

$$y_{ld} \approx Ax_0 + \epsilon_y, x_{ld} = \mathcal{R}(y_{ld}) = \underbrace{x_0 + bias}_{\mathcal{R}(Ax_0)} + \underbrace{\epsilon_x}_{\mathcal{R}(\epsilon_y)}, \quad (1)$$

where A is the projection matrix, ϵ_y is the projection noise, $\mathcal{R}$ is the reconstruction operator, and ϵ_x is the reconstruction noise term.

According to Noise2Noise [21], there is no need to pair clean and noisy data, only noise pair data can be recovered, i.e., a noisy data x_{ld} with another noisy data x'_{ld}'s as the target is equivalent to supervised learning on x_0. It can be expressed as:

$$\begin{aligned} &\min_{\theta} \left\{ \mathbb{E} \| f_\theta(x'_{ld}) - x_{ld} \|^2 \right\} \\ &\approx \min_{\theta} \left\{ \mathbb{E} \| f_\theta(x'_{ld}) - x_0 \|^2 + \mathbb{E} \| x_{ld} - x_0 \|^2 \right\} \end{aligned} \quad (2)$$

where $f_\theta(\cdot)$ represents a neural network driven by θ. However, this method requires two independent noise measurements of the same information and is not strictly self-supervised.

On this basis, Noise2Self [36] enriches the J-invariant theory to focus the research direction on the input x_{ld}. Noise2Void [37] and Noise2Same [38], on the other hand, focus on masking part of the image features by using the blind spot technique and constructing a corrupted set of images by using a specific neural network. Noiser2Noise [39] adds extra noise to the noise-containing images with additional noise to form training pairs. Neighbor2Neighbor [40], [41], on the other hand, is a simple and effective method to supervise each other by dividing neighboring subsamples from a single noisy data. Recorrupted2Recorrupted [42] keeps all the pixels intact and achieves self-supervised denoising by deriving two additional corrupted signals. However these methods usually unfold based on the independence of noise in the natural image. In the CT image domain, log transformations, interpolation and filtering during reconstruction change the noise distribution and introduce spatial correlation, leading to degradation of the performance of these methods.

For this reason, some researches have been carried out on noise optimization in CT, Niu *et al.* [22] proposed to use the similar data of each patient as the denoising target, but the randomness of the selected target can easily lead to too much similarity and reduce the denoising performance, while Wang

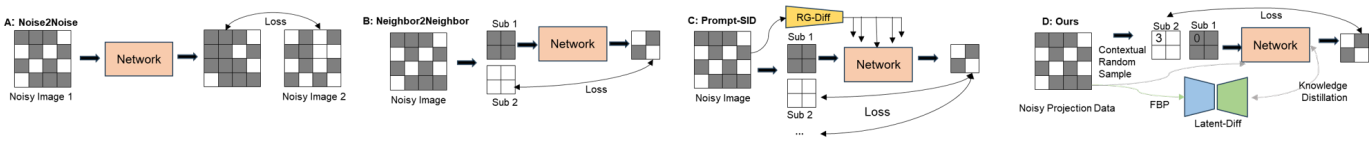

Fig. 1. Differences between SuperDiff and Noise2Noise, Neighbor2Neighbor, Prompt-SID.

et al. [43] optimized the selection scheme of the similar target and designed a new visual blind spot techniques to solve this problem. However, these methods are based on batch data, and have certain requirements on Z-axis CT data alignment. In addition, some novel researches have been carried out on the CT imaging principle, Wu *et al.* [44] proposed to utilize the unsharpened structure of the CT image domain to realize the self-supervised denoising by guided filtering, and proved that it is reasonable to start from the projection domain, and Proj2Proj [45] realized self-supervised denoising in the projection domain, and confirmed the feasibility of the same.

B. Application of Diffusion Models

The diffusion model, as a generative model obeying a Markov chain, is designed to learn an approximate distribution of the data in the forward noise addition and inverse denoising process. The forward process is constructed by adding noise to the given target data:

$$q(x_t|x_0) = \mathcal{N}\left(x_t; \sqrt{\bar{\alpha}_t}x_0, (1-\bar{\alpha}_t)\boldsymbol{I}\right), \tag{3}$$

$$x_t = \sqrt{\bar{\alpha}_t}x_0 + \sqrt{1-\bar{\alpha}_t}\epsilon, \epsilon \sim \mathcal{N}(0, \boldsymbol{I}), \tag{4}$$

where $\bar{\alpha}_t$ is a hyperparameter that controls the noise level, and the forward process adds noise up to $x_T \sim \mathcal{N}(0, \boldsymbol{I})$. The backward process then progressively predicts from x_T until it approaches x_0.

$$p_\theta(x_{t-1}|x_t) := \mathcal{N}(x_{t-1}; \boldsymbol{\mu}_\theta(x_t, t), \sigma_t^2\boldsymbol{I}), \tag{5}$$

$$\boldsymbol{\mu}_\theta(x_t, t) = \frac{1}{\sqrt{\alpha_t}}\left(x_t - \frac{1-\alpha_t}{\sqrt{1-\bar{\alpha}_t}}\epsilon_\theta(x_t, t)\right), \sigma_t^2 = 1-\alpha_t, \tag{6}$$

where ϵ_θ is a noise predictor driven by a neural network. The denoised image during sampling according to the above parameters per time t can be described as:

$$\tilde{x}_0 = \frac{x_t - \sqrt{1-\bar{\alpha}_t}\epsilon_\theta(x_t, t)}{\sqrt{\bar{\alpha}_t}}. \tag{7}$$

Recently, a series of extension studies have been carried out around the diffusion model, Song *et al.* [27] proposed that the score-based generative model can be used as the solution of stochastic equations (SDEs), Gao *et al.* [46] designed a diffusion model CoreDiff based on cold diffusion, which maintains physical degradation properties of the mean value. Based on this study, combined with the principle of scanning of the projection domain, the dual domain model NEED [47] was proposed, whose diffusion process becomes offset Poisson diffusion, and the dual guided diffusion was introduced in the image domain to optimal reconstruction of images. Liao *et al.* [31] designs a dual-domain denoising model that can reconstruct the image by iterating the part of the diffusion model, which optimizes the problem of the sampling efficiency of the traditional diffusion model. Yang *et al.* [48] proposes an efficient latent feature-guided diffusion model that can be applied to visible and infrared image fusion, medical image fusion and other scenarios. Li *et al.* [49] extracts structural representations from noise-containing images in the latent space based on cue learning to guide the restoration process, introduces a scale replay training mechanism, effectively mitigates the scale gap between images of different resolutions, and realizes the combined diffusion model with a dual domain denoising model with a low sampling efficiency. The scale gap is effectively mitigated between images of different resolutions, and self-supervised denoising in natural images combined with diffusion model is realized. Fig. 1 illustrates the self-supervised denoising research evolution process.

III. Method

In this section, we first introduce the denoising model for the upper and lower subgraphs of the LDCT projection domain. Subsequently, the latent diffusion model image refinement model based on a priori information is presented. Finally, the denoising process of the dual-domain denoising model in this study is described, and the importance of the bootstrap term in the reconstruction process is emphasized. Meanwhile, the pixel-level self-correcting fusion as well as the generalization strategy of the upper and lower doses are described in detail. The overall flowchart is shown in Fig. 2.

A. Projection Domain Contextual Sub-data Denoising

At present, the noise generated in the LDCT scanning process mainly comes from the quantum noise caused by photon fluctuation and the electronic noise caused by the equipment itself. And the image domain data under the filtered backprojection is prone to bring stronger spatial correlation. According to Eq. (2), following the noise-to-noise principle can realize that targeting noise is equivalent to recovering to a clean image. To this end, this study proposes a randomized contextual subdata sampling strategy $s(\cdot)$. Firstly, the noise-containing projection $y_{ld} \in \mathbb{R}^{H_y \times W_y \times C_y}$ is divided into $H_y/2 \times W_y/2$ chunks, each chunk contains four data points, and one point is randomly selected among the four data points i, the remaining three are the lower data point $i-1$ or the upper data point $i+1$, $i+2$ of that point, when $i=0$ or $i=3$ there is only the upper data point or the lower data point. As shown in Fig. 3, the selected data points are divided into different sampling data, and this contextual sub-data can be described as $s_1(y_{ld})$, $s_2(y_{ld})$, $s_3(y_{ld})$, with pixel resolutions of $H_y/2 \times W_y/2$. Meanwhile, a randomization strategy is

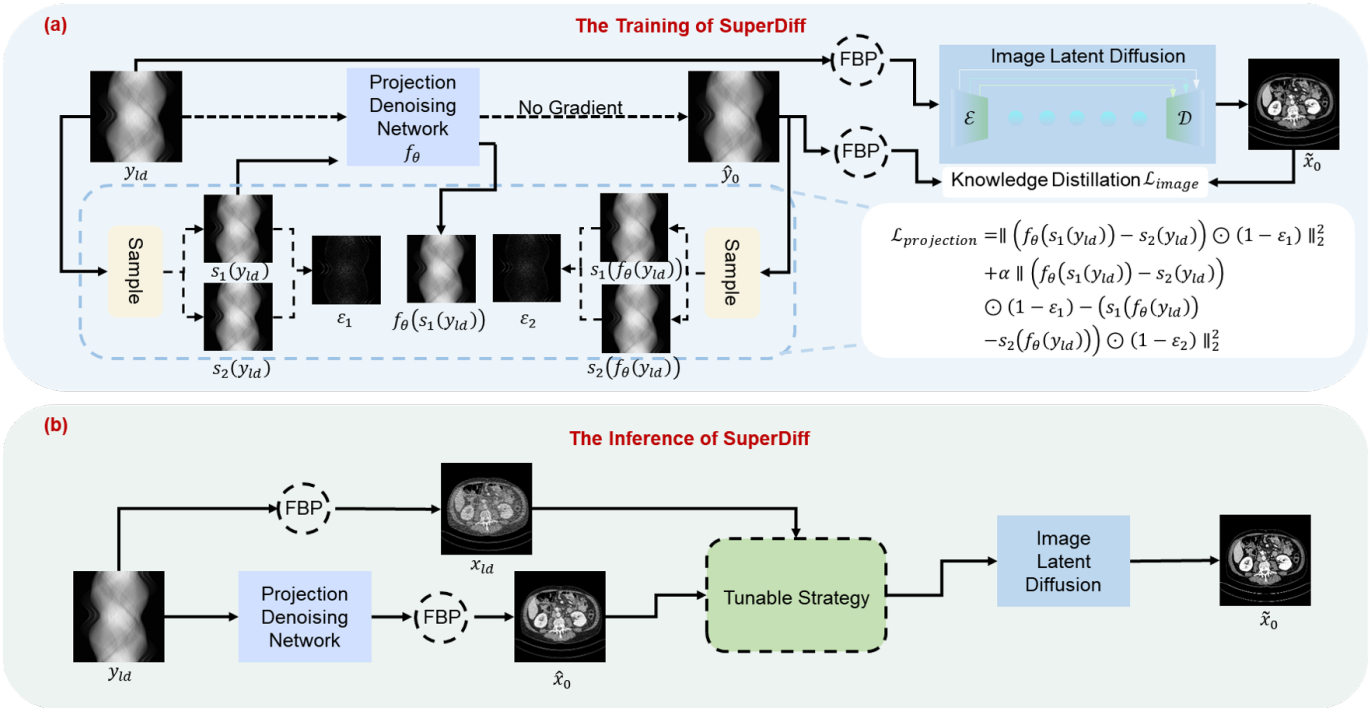

Fig. 2. General Architecture of SuperDiff Training and Inference.

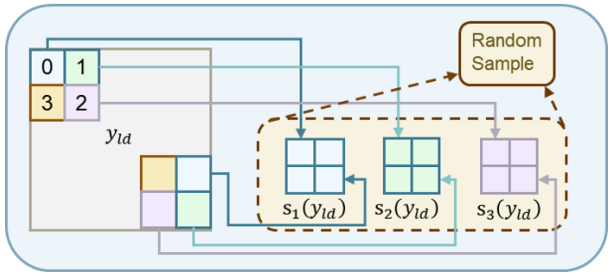

Fig. 3. Description of random sampling of contextual projection data.

adopted in order to select pairs of sub-data for training:

$$(s_i(y_{ld}), s_j(y_{ld})) \sim \mathcal{U}\left\{s_1(y_{ld}), s_2(y_{ld}), s_3(y_{ld})\right\}, \quad i \neq j, \tag{8}$$

where $(s_i(\cdot), s_j(\cdot)) \sim \mathcal{U}(\cdot)$ represents the sub-data of context features after uniform sampling.

According to Lemma 1 of [21], and the proof of [50]. Assuming that noisy image pairs a and b are conditionally independent given a clear image x, and that the gap between the two is defined as $\varepsilon := \mathbb{E}_{b|x_0}(b) - \mathbb{E}_{a|x_0}(a)$, the relationship between the noisy data pairs and the supervised training loss is defined as:

$$\begin{aligned}\mathbb{E}_{x_0,a} \parallel f_\theta(a) - x_0 \parallel_2^2 = \mathbb{E}_{x_0,a,b} \parallel f_\theta(a) - b \parallel_2^2 \\ - \sigma_b^2 + 2\varepsilon \mathbb{E}_{x_0,a}(f_\theta(a) - x_0),\end{aligned} \tag{9}$$

where σ_z^2 is the variance of b, and optimizing $\mathbb{E}_{x_0,a,b} \parallel f_\theta(a) - b \parallel_2^2$ is equivalent to optimizing the supervised loss when $\varepsilon \to 0$, and can yield an approximate solution for the supervised training network. Similarly, the pixel points of $s_1(y_{ld})$ and $s_2(y_{ld})$ are contextualized pixels in y_{ld}, which are similar as well as dissimilar in the latent real projection data y_0.

In order to highlight the similarity between the attention data, the parts with large gaps between the contextual sub-data maps are dynamically eliminated. This study proposes a spatial data self-enhancing similarity strategy, where the term pairs $(s_1(y_{ld}), s_2(y_{ld}))$ and $(s_1(f_\theta(y_{ld})), s_2(f_\theta(y_{ld})))$ are defined to satisfy the relations $\varepsilon_1 = \mathbb{E}_{y_{ld}|y_0}(s_1(y_{ld})) - \mathbb{E}_{y_{ld}|y_0}(s_2(y_{ld}))$ and $\varepsilon_2 = \mathbb{E}_{y_{ld}|y_0}(s_1(f_\theta(y_{ld}))) - \mathbb{E}_{y_{ld}|y_0}(s_2(f_\theta(y_{ld})))$, respectively. After extracting the regions of difference, the model dynamically broadcasts the result to the supervision loss calculation. Therefore, the objective function at this stage can be defined as:

$$\begin{aligned}\min_\theta \mathbb{E}_{y_0,y_{ld}} \parallel (f_\theta(s_1(y_{ld})) - s_2(y_{ld})) \odot (1-\varepsilon_1) \parallel_2^2 \\ + \alpha \mathbb{E}_{y_0,y_{ld}} \parallel (f_\theta(s_1(y_{ld})) - s_2(y_{ld})) \odot (1-\varepsilon_1) \\ - (s_1(f_\theta(y_{ld})) - s_2(f_\theta(y_{ld}))) \odot (1-\varepsilon_2) \parallel_2^2,\end{aligned} \tag{10}$$

where $\odot$ represents element-by-element multiplication and α is empirically set to 0.02. For detailed information about Eq. (10), please refer to the Appendix.1.

The initial denoised projection data $\hat{y}_0$ can be obtained after the above processing. It is worth noting that only LDCT projection data is involved in this stage of the training process. The initial reconstructed image domain $\hat{x}_0$ can be described as:

$$\hat{x}_0 = \mathrm{FBP}(\hat{y}_0). \tag{11}$$

B. Latent Diffusion Image Refinement

Although the denoising stage under the projection domain can substantially reduce the noise, the initial reconstruction $\hat{x}_0$ may suffer from blurring and insufficient denoising, and therefore, it needs to be optimized again under the image domain. However, if it is processed again through the

projection domain approach, it may accumulate errors due to excessive correlation in the CT image domain, deviate from the correct optimization gradient, and experience severe information corruption. To solve this problem we introduce a denoising framework based on the latent diffusion model, with the help of its Gaussian diffusion to learn the uncorrupted feature information in the latent space for refining the image features.

The traditional latent diffusion model (LDM) needs to pre-train the encoder with the help of clean images to adapt to different tasks, however, this is not in line with the original intention of self-supervised denoising from a single projection domain. Fortunately, Yang *et al.* [48] proposes to use U-Net as encoder and decoder to solve this problem perfectly, which can both map the information to the latent space to reduce the complexity and computational cost, and fully perceive the high-frequency noise in the noisy image. From Eqs. (3) (4) (5), a preliminary knowledge of diffusion modeling can be obtained, and for better work, the submerged diffusion model is defined as below:

$$x_{ld}^{L} = \mathcal{E}(x_{ld}), \tag{12}$$

$$\tilde{x}_0 = D(x_0^L), \tag{13}$$

where $\mathcal{E}$ represents the pixel-level encoder used to map x_{ld} to the latent space variable x_{ld}^L. The x_0^L represents the latent space variable to be decoded after denoising. The $\mathcal{D}$ is then the decoded compression variable x_0^L for the final denoised CT image $\widetilde{x}_0$.

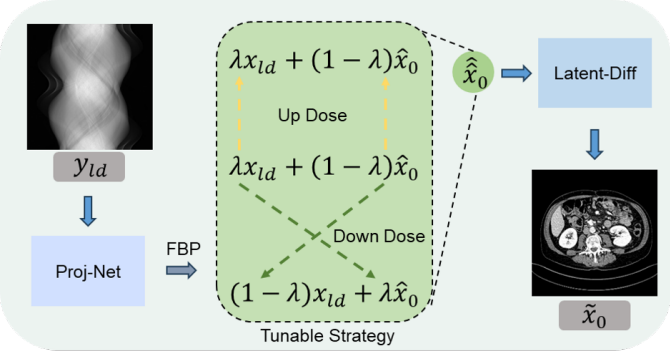

Fig. 4. Tunable up- and down-dose generalization strategy.

In order to utilize the intermediate representation a priori information of the initial reconstruction $\hat{x}_0$, this study introduces the information distillation technique to be deeply integrated with the LDM model architecture. 1) Use the pre-trained projection domain model to obtain $\hat{x}_0$, which exists as a representation constraint a priori. 2) Compress x_{ld} into a low-dimensional space via Eq. (12), while performing forward re-degradation to a random Gaussian noise x_T via Eq. (3), after which train a noise prediction network $\epsilon_\theta(\cdot)$ via Eq. (5) to perform inverse denoising until generating x_0^L, after which decoding is performed via Eq. (13) for decoding. 3) After the above operation, the $\hat{x}_0$ of 1) is used as a constrained prior to update the result of 2) continuously through iterative training, to compensate for some of the missing details in $\hat{x}_0$. It is noteworthy that $\epsilon_\theta(\cdot)$ takes the transformer as the framework of the noise prediction network, which can better play the role of long-range dependence focusing on low-frequency information. And the 5-step sampling of the inverse process greatly improves the reconstruction efficiency. Therefore, the loss in this stage contains diffusion loss and denoising loss:

$$\mathcal{L}_{\text{image}} = \mathcal{L}_{\text{diff}} + \mathcal{L}_{\text{denoising}}, \tag{14}$$

during training, the loss can be composed of the above, where $\mathcal{L}_{\text{diff}}$ represents minimizing the difference between the denoising network prediction noise $\epsilon_\theta(x_t, t)$ and the initial sampling noise ϵ:

$$\mathcal{L}_{\text{diff}} = \left\|\epsilon - \epsilon_\theta(x_t, t)\right\|^2, \tag{15}$$

where x_t is obtained from Eq. (4) after several forward degenerations. The denoising loss aims to give full play to the role of information distillation to achieve refinement of details and information compensation. It can be defined as:

$$\begin{aligned}\mathcal{L}_{\text{denoising}} &= \beta\mathcal{L}_{\text{ssim}} + \gamma\mathcal{L}_{\text{grad}} + \eta\mathcal{L}_{\text{l1}} \\ &= \beta\left(1 - \text{ssim}(\mathcal{D}(x_t^L), x_0)\right) \\ &+ \gamma\frac{1}{H_x W_x}\left\||\nabla\hat{x}_0| - |\nabla D(x_t^L)|\right\|_1 \\ &+ \eta\frac{1}{H_x W_x}\left\|\hat{x}_0 - \mathcal{D}(x_t^L)\right\|_1,\end{aligned} \tag{16}$$

where β, γ, η represent the weights of each loss, which are empirically set to 1.0, 2.0, 0.5. ∇ represents the Sobel-based gradient operator. The $\|\cdot\|_1$ represents the l_1 paradigm. x_t^L represents a certain latent state that is not fully denoised. H_x and W_x represent the height and width of the image domain, respectively.

C. Pixel-level Fusion Reconstruction and Tunable Generalization for Up- and Down-dose

1) Pixel-level self-correcting fusion reconstruction: A trained projection domain model and an image domain model using a single projection domain are used for LDCT dual-domain reconstruction. When the dual-domain model cascade is performed for reconstruction, if the initial reconstruction $\hat{x}_0$ in the projection domain is used as the starting point of the image domain stage, it may have the effect of over-suppressing the noise and destroying the medical lesions. For this reason, we introduce a weighted fusion of x_{ld} and $\hat{x}_0$ for guiding the reconstruction of the image domain in the inference stage, which can avoid introducing excessive noise and artifacts while compensating for the information lost in the projection domain stage. However, the weighted fusion in previous studies usually uses fixed weights, and even if adaptive weights are used, they exist as varying single values, all failing to take into account the non-uniform variations of noise and features.

Therefore, this study adopts weights for each pixel point for x_{ld} and $\hat{x}_0$ self-corrected weighted fusion. Specifically, local noise level estimation and gradient magnitude computation are first performed for x_{ld} and $\hat{x}_0$, respectively, and the pixel-level

self-correcting weight λ is subsequently computed from the confidence level of both. The description is as follows:

$$C_e = \sigma(k_2(G_{\hat{x_0}} - \tau_e)), C_n = \sigma(k_1(N_{x_{ld}} - \tau_n)), \quad (17)$$

$$\lambda = \text{Clip}(C_e + C_n, 0, 1), \quad (18)$$

where C_e and C_n are the edge confidence and noise confidence. $\sigma(z) = \frac{1}{1+e^{-z}}, k_1, k_2 > 0$ and $\tau_e = 0.15, \tau_n = 0.3$. $G_{\hat{x}_0}$ is the gradient magnitude and $N_{x_{ld}}$ is the noise level estimate. The $\lambda \in \mathbb{R}^{B_x \times C_x \times H_x \times W_x}$ exists as pixel-level weights. So the image into the image domain is represented as:

$$\hat{\tilde{x}}_0 = \underbrace{\lambda x_{ld}}_{\text{LDCT term}} + \underbrace{(1-\lambda)\hat{x}_0}_{\text{middle term}}, \quad (19)$$

where λ must not be all 1, otherwise this is contrary to the original purpose of cascading dual-domain denoising, $\hat{\tilde{x}}_0$ is the image to be denoised into the image domain pre-training model, and then denoised by the Eq. (16) pre-trained model to get our final reconstructed image $\tilde{x}_0$.

2) Adjustable strategies of upper and lower dose generalization: Previous studies have shown that taking deep learning for self-supervision although does not require the involvement of paired and clean data but requires different doses of data for training and testing. And the reconstruction effect decreases significantly when the model of the same dose is exposed to another dose. Therefore, this study proposes a weight correction adjustment generalization scheme for dosages above or below the current training dose while generalizing the significant effect of different doses. Specifically, taking the 25% dose training as an example, x_{ld} is used as the starting point of image domain training as mentioned in Section 2 of the method, and the weight share of x_{ld} in the inference process should be high to match the training gradient. For the lower dose, with more noise than the 25% dose, the weight share should be more in favor of $\hat{x}_0$, and similarly, for the upper dose, less noise should be in favor of x_{ld}. Overall, the generalization process performs the weight replacement in Eq. (19) according to the noise strength,as shown in Fig. 4.

Algorithm 1 Training Process

Input: Single LDCT projection data y_{ld}, densigned $s(\cdot)$, total time steps T and sampling steps T_L;
Output: A well-trained f_θ, $\mathcal{E}$, $\mathcal{D}$ and ϵ_θ;

Repeat:
  Calculate $s_1(y_{\text{ld}})$, $s_2(y_{\text{ld}})$ by Eq. (8);
  Update f_θ by Eq. (10);
  Update $\mathcal{E}$, $\mathcal{D}$, ϵ_θ by Eq. (14);
Until converged;

IV. Experiments

This section focuses on the dataset used in this study, the simulation approach, the experimental details, and the evaluation metrics. Subsequently, the proposed method is thoroughly evaluated by quantitatively and qualitatively comparing it with the current state-of-the-art denoising methods. Next, the method is applied to a real clinical scenario for validation.

Algorithm 2 Inference Process

Input: Single LDCT projection data y_{ld}, a well-trained f_θ of the projection domain, a well-trained $\mathcal{E}$, $\mathcal{D}$ and ϵ_θ of the image domain, total time steps T and sampling steps T_L;
Output: Reconstructed image $\tilde{x}_0$;

$\hat{y}_0 \leftarrow f_\theta(y_{ld})$;
Calculate $\hat{x}_0$ by Eq. (11);
Calculate $\hat{\tilde{x}}_0$ by Eq. (19);
$\hat{\tilde{x}}_0^L \leftarrow \mathcal{E}(\hat{\tilde{x}}_0)$;
for $t = T, T-(T/T_L), \cdots, 1$ **do**
  Calculate $\hat{\tilde{x}}_{t-1}^L$ by Eq. (5);
end for
Caluculate $\tilde{x}_0$ by Eq. (13);

Finally, ablation experiments are designed to verify the validity of this study.

A. Datasets

1) Mayo dataset: The Mayo dataset [51] from AAPM Grand Challenge was used to validate the algorithms, which consisted of the NDCT data and the corresponding simulated LDCT data from 10 patients. In this study, in order to obtain data at different doses, a simulated LDCT method similar to the study of [52] was used. It can be described as:

$$y_{ld} = \ln \frac{I_0}{\text{Poisson}(I_0 \exp(-y_0)) + \text{Gaussian}(0, \sigma_e^2)}, \quad (20)$$

where y_{ld} and y_0 represent low-dose and regular-dose fan-beam log projection data, respectively. I_0 was set to 1.5×10^5 as the simulated incident photon number for this study. The σ_e^2 represents the electronic noise variance, which is set to a fixed value of 10. The source-to-rotation center distance was 1361.2 mm, and the detector-to-rotation center distance was 615.18 mm. A total of 720 views were acquired within a 360-degree acquisition range. Finally, the image domain data were obtained after FBP with a pixel resolution of 512×512. A total of 50%, 25%, and 10% doses of data were simulated for training and testing in this study. After the above processing, we selected 8 cases for training and 2 cases ($L067$,$L096$) for testing.

2) LIDC-IDRI dataset: To further validate the model, this study utilized the publicly available dataset LIDC-IDRI (Lung Image Database Consortium and Image Database Resource Initiative) [53]. It is a publicly available lung nodule dataset, which is mainly used to study early cancer detection in high-risk populations. The dataset contains a total of 1018 lung CT scan images from 1010 lung patients. After preprocessing, a simulation approach similar to that of the Mayo dataset was taken to derive 25%, 10% dose data. Finally 45 patients were selected for training and 5 patients for testing.

3) Real clinical dataset: The real clinical data contained a total of 500 LDCT image domain images with a pixel resolution of 512×512 and a projection domain of 720×720. These data were acquired using a GE scanner (Discovery CT750 HD) at 120 kVp, 80 mAs and 1.25 mm slice thickness. In this paper, real clinical data were used only for testing to verify

the generalizability and validity of this study in real LDCT. To be precise, real data were tested directly using models trained on the LIDC-IDRI dataset.

B. Implementation Details

The main structure of the contextual sub-projection domain stage model is similar to the U-Net architecture of [54], with the two downsampling stages removed to accommodate the projection domain size. An Adam optimizer with an initial learning rate of 0.0003 is used, the training batch size is set to 8, the total training epochs are set to 100, and the learning rate is halved every 20 epochs. Both the self-encoder and decoder in the reconstruction stage of latent diffusion image optimization have four layers, and the denoising network based on the transformer architecture also has four layers. For the diffusion training process, the AdamW optimizer with an initial learning rate of 0.0003 is used for optimization and the learning rate is adjusted according to the cosine return algorithm, with $T = 1000$ diffusion steps, $T_L = 5$ sampling steps, 4 training batch size, and a total training period of 60. All the training and testing experiments are performed on the PyTorch platform using NVIDIA RTX 4090D GPU (24GB). The projection domain phase took about 5 hours and the image phase took about 20 hours. Source code is made available at https://github.com/yqx7150/SuperDiff.

C. Comparison Methods

In order to evaluate the state-of-the-art of this study, we selected traditional denoising methods and several self-supervised/unsupervised methods for comparison. These include 1) Total Variation (TV) [55], 2) B2U [56], Neighbor2Neighbor (NBR) [40], Noiser2Noise [39], Prompt-SID [49], Noise2Sim [22], AdaReNet [57], IPDM [31]. Where AdaReNet is another variant based on Noise2Noise introducing a prior such as rotation in the network, which also requires the same information for the unfolding of noise pairs. For this reason, 10% and 25% doses are selected for training, while IPDM is a type of unsupervised learning that requires the involvement of clean data, for which the bi-domain approach is taken to unfold strictly as described in the paper. For all of the above methods, we refer to the original paper for comparison experiments, except for TV and IPDM, for which the batch size is 1, the batch size is 4 and the epoch is 60.

D. Evaluation Metrics

In order to assess the superiority of the methodology in this study, three well-established metrics were selected for quantitative evaluation: peak signal-to-noise ratio (PSNR), structural similarity (SSIM) [58] and root mean square error (RMSE). In order to validate the clinical feasibility of the method, three other metrics that are close to the radiologist's judgment of the condition were introduced in this study: feature similarity index (FSIM) [59], visual information fidelity (VIF) [60], and noise quality metric (NQM) [61]. The higher the PSNR, SSIM, FSIM and VIF, the better, and the lower the RMSE and NQM, the better. All metrics were calculated under the CT window [-1024,3072] HU.

E. Experiment Results

1) Evaluation of different datasets: In this study, the superiority of the present model is demonstrated by quantitatively evaluating the Mayo and LIDC-IDRI datasets with 25% dose, respectively. In the other experiments of the comparison, we have taken the traditional method, self-supervised and clean data based iterative diffusion method, which can reflect the advancement of the present method from several angles, which is clearly demonstrated in Fig. 5 from the image itself, zoomed-in and residual maps. The traditional TV, although it can realize the noise removal, has transitional smoothing and destruction of pathological features, and the parameter settings are non-uniform for different data and system devices. Deep learning-based methods, such as B2U, suffer from performance degradation due to their inability to adapt to the overly structured and correlated noise in CT images. Noiser2Noise tends to introduce too much random noise due to the introduction of additional noise in the noisy image itself in order to construct a supervised image, appearing to smooth out textures and details similar to TV methods. In addition, Prompt-SID, which is based on cue learning and introduces a diffusion model to amplify the perceptual noise, did not show eye-opening results on the Mayo dataset. NBR, which fails to introduce enhancement for similarity as our method, produces lesions that do not stand out as shown in Figs. 5 and 6, both in the lungs and in the abdomen. As can be seen from Table I, Noise2Sim, AdaReNet, and IPDM all showed good results, but Noise2Sim's method based on batch data similarity requires higher data z-axis orientation, which resulted in a significant drop in metrics across different datasets, and the overly randomized selection of similar data can easily lead to drifting of CT values as shown in Figs. 5 and 7. However, our method mitigates the CT value mismatch due to the pixel-level weighted correction that achieves a balance in suppressing noise and preserving details. Notably, although the effect on the LIDC data is lower than that of AdaReNet, it requires independent noisy data with the same information, which cannot be strictly classified as self-supervised, and as shown in Fig. 7, the image produces a smoothing of the details on the muscle tissues and bones, which can interfere with the diagnostic performance of the radiologist to a large extent. For IPDM's approach based on iterative diffusion over two domains starting from clean data, which mitigates the presence of noise at the cost of a huge cost, although modeling with clean data has a great advantage, it is still not sufficient for feature recovery. As shown in the folded line in Fig. 5, our method is closest to the reference in terms of amplitude variation, which fully demonstrates the robustness of the present method in denoising reconstruction. In addition, it is worth emphasizing that our method only requires single LDCT projection data, whether training or testing the model, which is a real self-supervised method that this study aims to address when a large number of labels are missing in the clinic.

2) Experimental results on tunable generalization: Self-supervised based methods are commonly associated with a significant decrease in generalization effect when the pre-

TABLE I

QUANTITATIVE RESULTS (MEAN±STD) ON 25% DOSE LEVEL FROM THE MAYO 2016 DATASET AND THE LIDC-IDRI DATASET. THE BEST RESULTS ARE HIGHLIGHTED IN BOLD.

Methods	Mayo Dataset						LIDC-IDRI Dataset					
	PSNR ↑	SSIM(%) ↑	RMSE ↓	FSIM(%) ↑	VIF(%) ↑	NQM ↑	PSNR ↑	SSIM(%) ↑	RMSE ↓	FSIM(%) ↑	VIF(%) ↑	NQM ↑
Baseline/Tradition												
FBP	31.89±2.58	70.00±10.27	53.17±15.93	94.74±2.73	24.60±7.51	28.06±2.89	36.39±3.43	84.28±9.91	32.73±14.90	96.84±2.30	37.10±13.74	31.35±2.69
TV	38.21±2.47	94.30±2.49	24.74±9.21	95.31±1.31	61.21±13.52	22.03±2.68	40.05±1.31	96.03±0.82	20.03±3.61	94.68±3.10	62.10±9.80	28.14±1.51
Self-supervised												
B2U	32.83±2.39	73.41±9.69	47.44±13.66	96.02±2.04	26.29±8.17	26.86±2.55	36.78±3.61	85.22±9.80	31.58±13.07	97.10±2.17	39.29±14.94	30.02±2.59
Neighbor2Neighbor	39.02±2.35	92.41±3.92	23.25±6.79	98.22±0.81	53.37±11.39	27.47±2.58	41.59±2.40	96.01±2.61	17.32±5.28	98.68±0.63	64.41±13.60	30.65±2.38
Noiser2Noise	38.22±2.53	92.52±5.24	25.78±9.42	97.05±0.63	61.58±12.84	24.28±1.15	38.34±0.95	96.15±0.97	24.33±2.69	96.91±0.69	67.62±4.61	21.39±0.79
Prompt-SID	36.71±2.51	87.21±6.03	30.47±9.20	98.05±0.99	41.72±10.78	28.18±2.58	40.43±2.77	94.05±3.97	20.04±6.78	98.86±0.70	56.37±14.73	31.42±2.32
Noise2Sim	39.32±1.42	95.68±0.92	21.92±3.84	97.86±0.47	65.04±5.95	26.18±2.87	36.70±2.33	95.99±0.71	30.36±9.17	97.21±0.71	64.39±7.62	20.68±3.63
AdaReNet	40.80±3.56	96.47±0.32	20.44±13.33	98.43±0.13	72.41±6.04	28.21±3.29	**43.47±0.64**	97.90±0.55	14.56±2.47	**99.14±0.12**	76.34±2.79	**32.33±1.21**
Unsupervised												
IPDM	41.32±0.99	96.78±0.80	17.81±3.61	98.45±0.43	72.90±4.80	28.07±2.28	42.30±0.74	97.84±0.55	15.39±1.36	98.36±0.36	75.30±4.76	30.32±1.30
Self-supervised												
Ours	**42.41±1.21**	**96.90±0.83**	**15.30±2.21**	**98.71±0.33**	**73.64±5.44**	**28.25±2.35**	42.85±0.77	**97.95±0.40**	**14.46±1.38**	98.95±0.23	**76.45±3.79**	31.54±2.11

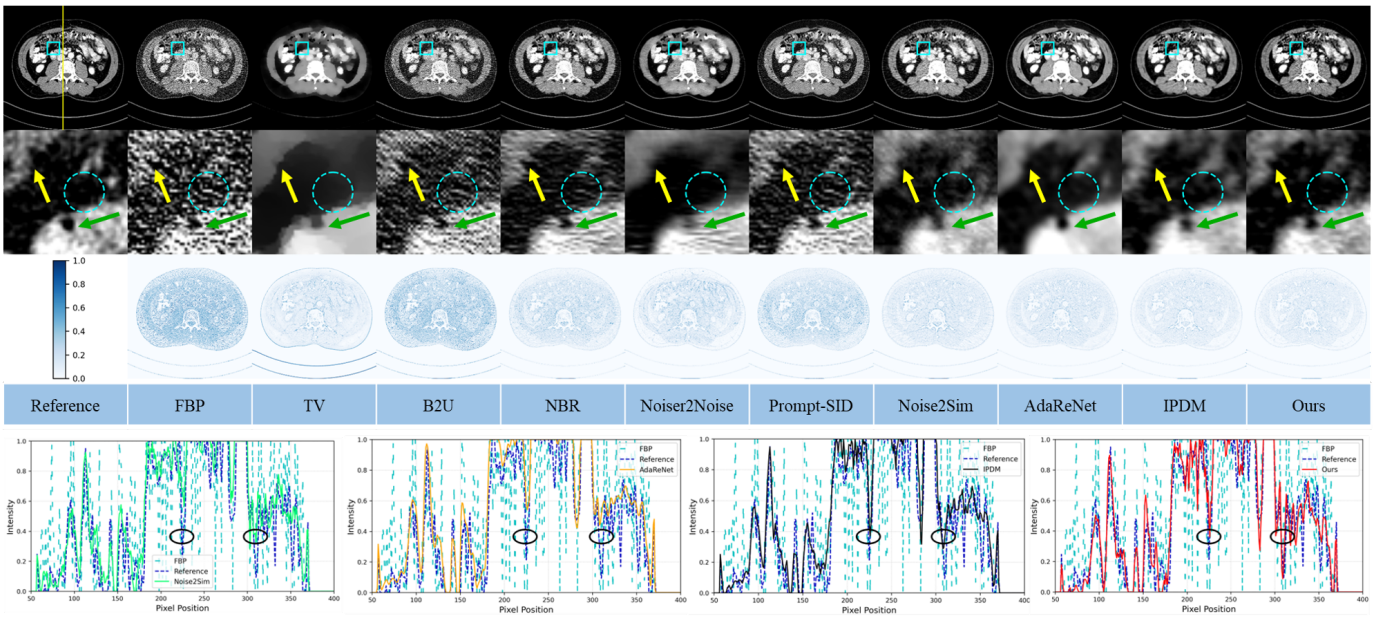

Fig. 5. Qualitative results of a 25% dose CT image from the Mayo dataset. quantitative assessment against the Mayo 25% dose dataset in the abdomen. The blue region of interest is zoomed in to demonstrate the difference, and the green and yellow arrows point to lesions with significant disparities. The line graphs show the fit of Noise2Sim, AdaReNet, IPDM, which are similar to the models in this study, to the reference in a column, respectively. The display window is [-100,200] HU.

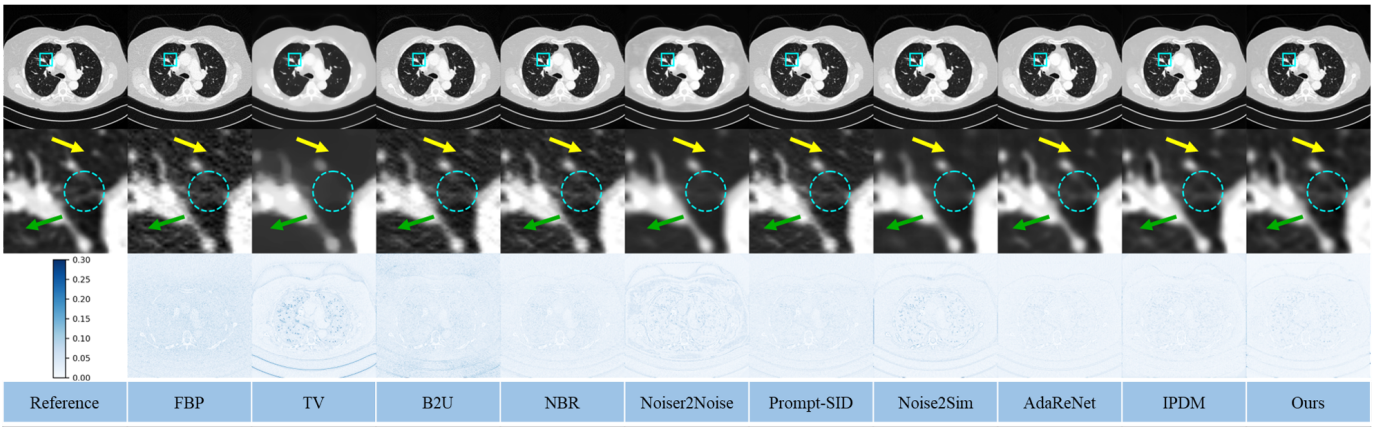

Fig. 6. Quantitative assessment in the lungs against the Mayo 25% dose dataset. The blue region of interest is zoomed in to show the difference, and the green and yellow arrows point to lesions with significant disparity. The display window is [-1350, 200] HU.

trained model of a single dose is applied to different doses, fortunately this study in demonstrated the feasibility and superiority of generalization at different doses. On the basis of this, we propose an adjustable generalization strategy for upper and lower doses as shown in Fig. 4 to maximize the model effect. As shown in Fig. 8 and Table II, for the generalization

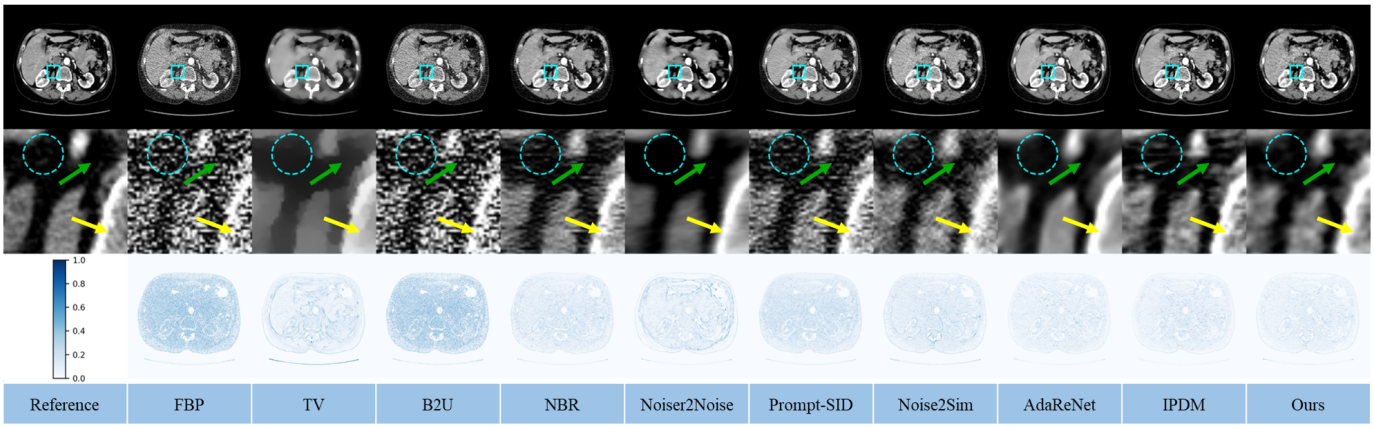

Fig. 7. Quantitative assessment against the LIDC-IDRI 25% dose data set in the abdomen. The blue region of interest is zoomed in to show the difference, and the green and yellow arrows point to lesions with significant disparity. The display window is [-100,200].

TABLE II

QUANTITATIVE GENERALIZATION RESULTS (MEAN±STD) ON DIFFERENT DOSES LEVEL FROM THE MAYO 2016 DATASET AND THE LIDC-IDRI DATASET. THE BEST RESULTS ARE HIGHLIGHTED IN BOLD.

Methods	Mayo Dataset 25% → 10%			Mayo Dataset 25% → 50%			LIDC-IDRI Dataset 25% → 10%			LIDC-IDRI Dataset → Mayo Dataset 25% → 50%		
	PSNR↑	SSIM(%) ↑	RMSE ↓	PSNR ↑	SSIM(%) ↑	RMSE ↓	PSNR ↑	SSIM(%) ↑	RMSE ↓	PSNR ↑	SSIM(%) ↑	RMSE ↓
Baseline/Tradition												
FBP	26.60±4.04	49.79±13.28	105.38±58.21	34.98±2.26	81.44±7.24	36.84±9.60	32.20±4.33	70.79±15.97	55.93±30.78	34.98±2.26	81.44±7.24	36.84±9.60
TV	38.21±2.47	94.30±2.49	24.74±9.21	39.41±1.20	85.24±6.20	24.83±2.68	39.05±1.21	80.03±0.34	40.03±3.61	39.41±1.20	85.24±6.20	24.83±2.68
Self-supervised												
B2U	29.94±4.51	68.75±12.36	73.50±43.38	37.36±2.24	89.23±5.01	28.03±7.55	34.56±4.52	81.32±11.77	43.59±28.67	36.93±2.22	88.20±5.35	29.44±7.84
Neighbor2Neighbor	34.13±4.67	82.13±10.58	46.30±30.85	41.13±1.67	95.59±1.83	17.88±3.62	38.31±4.28	91.06±7.06	28.31±20.77	40.62±1.75	94.95±2.24	19.00±4.06
Noiser2Noise	32.11±6.52	77.39±15.33	67.33±59.56	39.68±0.84	95.78±1.15	20.83±2.04	37.03±3.80	92.04±7.17	32.22±23.99	36.70±1.13	95.46±0.96	29.48±3.87
Prompt-SID	31.81±4.36	73.28±11.89	58.94±35.08	39.21±1.92	92.72±3.34	22.44±5.15	36.75±4.43	86.61±9.45	33.83±22.89	39.23±1.93	92.78±3.35	22.41±5.20
Noise2Sim	36.14±4.67	90.99±6.54	37.92±32.10	39.86±1.36	96.31±0.70	20.58±.56	35.73±3.17	93.91±3.35	35.61±19.40	36.24±2.42	95.51±1.10	32.04±9.05
AdaReNet	33.29±9.36	86.26±13.66	81.95±13.66	42.47±1.12	97.43±0.56	15.17±2.06	40.98±3.91	96.23±4.53	**20.31±16.27**	**42.13±0.64**	97.20±0.48	16.99±1.21
Unsupervised												
IPDM	38.02±4.27	91.46±9.27	29.53±22.78	41.93±0.76	97.35±0.52	16.07±1.43	40.59±3.10	95.73±3.83	21.30±11.05	41.57±0.70	97.18±0.61	16.73±1.39
Self-supervised												
Ours	**40.82±1.44**	**96.13±1.11**	**18.44±3.30**	**43.11±1.10**	**97.46±0.53**	**14.09±1.85**	**41.14±4.02**	**96.26±4.01**	20.95±20.06	41.85±0.98	**97.40±0.52**	**16.25±1.89**

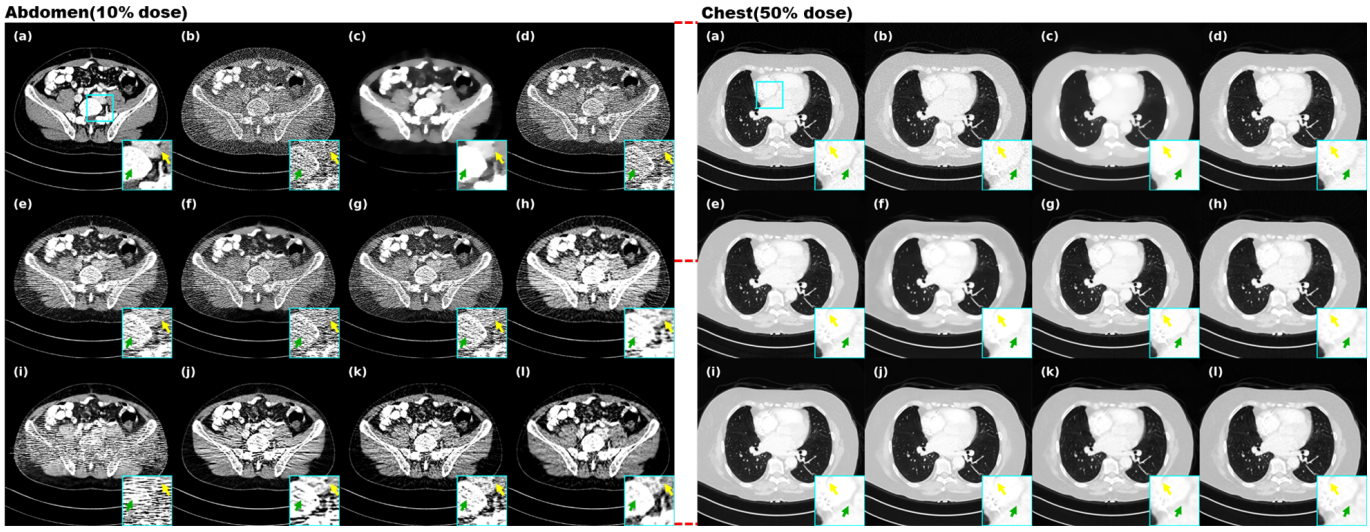

Fig. 8. Display of results on up and down dose generalization for (a) Reference (b) FBP (c) TV (d) B2U (e) NBR (f) Noiser2Noise (g) Prompt-SID (h) Noise2Sim (i) AdaReNet (j) IPDM (k) Ours-1 and (l) Ours-2. The abdomen is shown on the left and the lungs on the right.The display window for abdomen images is [-100, 200] HU and for chest images is [-1350,200] HU. The blue ROIs are zoomed in for visual comparison, and the yellow and green arrows point to key details.

of abdominal data for the lower dose 10% dose, this study presents a breakthrough lead in both numerical and image effects. For AdaReNet, although it performs slightly better than us for the lung data, it shows a discontinuous drop for the abdominal data, and our model even eliminates the shot noise due to the bones, which other methods do not have the ability to do. In addition, the difference between the upper and lower dose strategies exhibited in Fig. 8 is a good indication of the correctness of the generalization strategy for adjustability. Meanwhile, inspired by NEED [47], we also

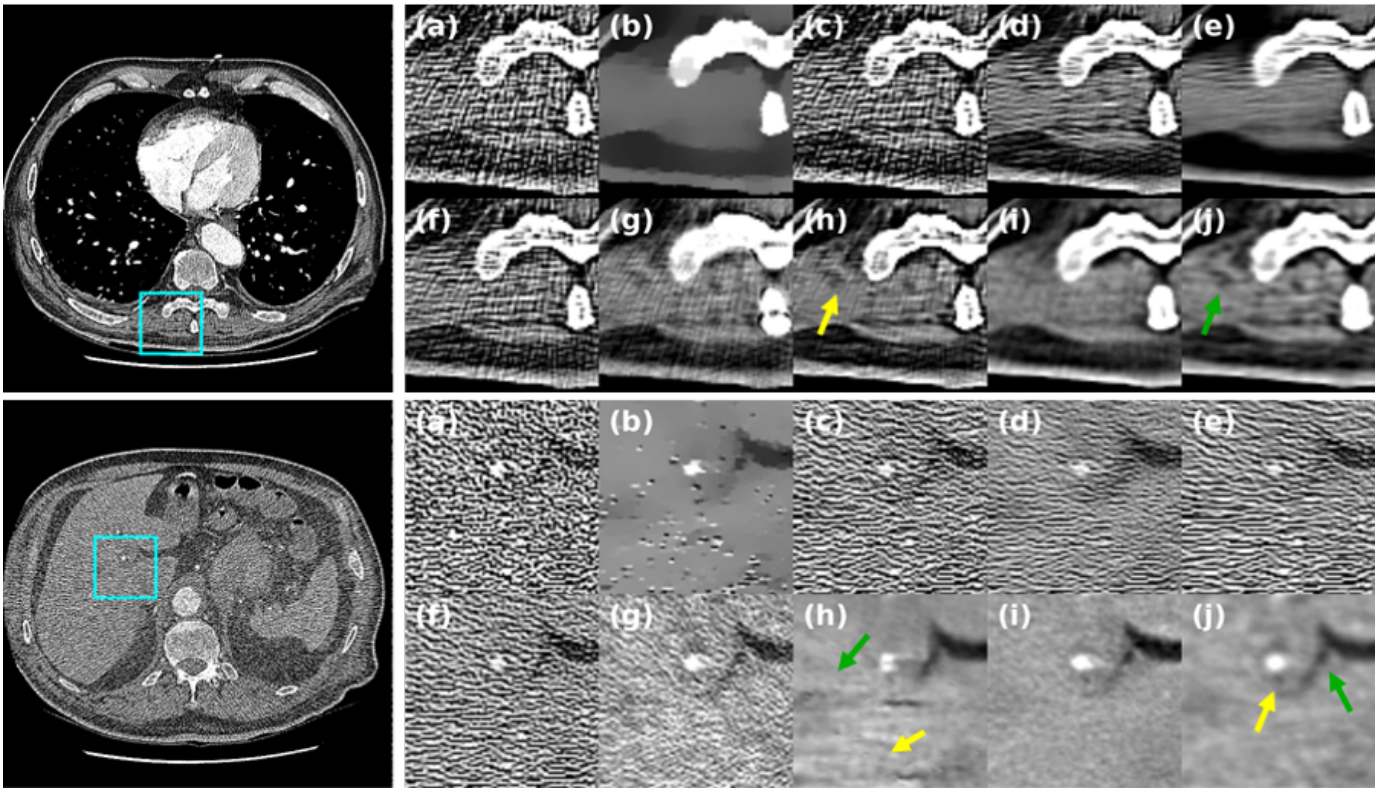

Fig. 9. Generalized results from real clinical data. (a) FBP (b) TV (c) B2U (d) NBR (e) Noiser2Noise (f) Prompt-SID (g) Noise2Sim (h) AdaReNet (i) IPDM (j) Ours. The display window is [-100, 200] HU.

apply this strategy to the LIDC-IDRI pre-trained model to generalize Mayo's data to validate the reconstruction ability on unseen datasets.

3) Representation of real clinical data: Since the data used for training and testing were obtained in a simulated manner, to better validate the clinical usability of the method, we took several cases from real patients for the study. The models used for analysis were trained on the LIDC-IDRI dataset. In order to better demonstrate the effectiveness of the generalization, the HU values of all datasets are unified. As shown in Fig. 9, our method compared to AdaReNet well recovers the detail part and removes the shot noise. The noise around the original lesion is effectively removed, which helps better clinical diagnosis. IPDM shows smoothing after double-domain processing, some details are missing, and generalization decreases. Noise2Sim noise masks the important parts. The other methods, although stronger than FBP, are insensitive to real data noise, resulting in degraded generalization performance. On the contrary, our SuperDiff removes the noise to a large extent and the pathological features are well reconstructed. It will bring a new paradigm to self-supervised denoising methods.

F. Ablation Study

1) Validity of the dual domain: In this study, we first analyze the model from the overall perspective, and for the process of denoising the LDCT projection domain first, followed by optimization of the image domain, we conducted ablation experiments for the single stage and the overall stage, respectively. As shown in Fig. 10 and Table III, the single-stage log projection domain denoising reveals that there is insufficient denoising for the noise, incomplete denoising of local muscle tissues, and some details of the skeleton are not fully recovered, and after the knowledge distillation in the image domain, the information is well recovered. This also shows that the initial reconstruction $\hat{x}_0$ and the original information x_{ld} both act as the guiding information for the reconstruction to check and fill in the gaps.

TABLE III
ABLATION STUDIES (MEAN±STD) ON THE PROPOSED MODULES ON 25% DOSE TEST DATA FROM THE MAYO DATASET.

Proj.	Imag.	PSNR ↑	SSIM(%) ↑	RMSE ↓
✓	×	41.11±1.07	95.52±1.03	17.73±2.28
✓	✓	**42.41±1.21**	**96.90±2.49**	**15.30±2.21**
Dissimilarity		PSNR ↑	SSIM(%) ↑	RMSE ↓
✓		41.09±0.87	95.46±0.62	17.52±1.79
×		**41.11±1.07**	**95.52±1.03**	**17.73±2.28**

2) Importance of adaptive enhancement of data similarity in log projection domain: After analyzing the effectiveness of the dual-domain phase, we focus on the proposed adaptive weighting strategy for data similarity in the projection domain phase. This strategy is proposed to shorten the dissimilarity between contextual sub-data to fit the theorem of the method part. So it focuses on highlighting the loss weight of similarity

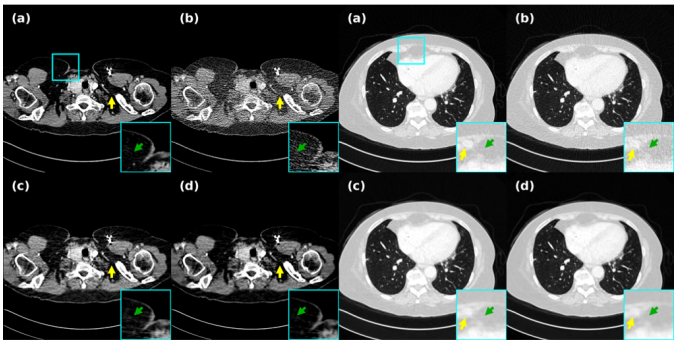

Fig. 10. Verification of ablation studies for two-stage effectiveness. (a) Reference (b) FBP (c) Only projection (d) Ours. The display window for abdomen images is [-100, 200] HU and for chest images is [-1350,200] HU. The blue ROIs are zoomed in for visual comparison, and the yellow and green arrows point to key details.

and ignoring the excessive part of dissimilarity. Fig. 11 and Table III show that the feature information of the image recovered after this strategy is well-defined, whereas not taking this strategy presents the effect of feature smoothing and gradient disappearance. This can lead to the subsequent refinement stage of the image domain not being able to discriminate well between the noise information and the organizational structure, and falling into a sub-optimal situation.

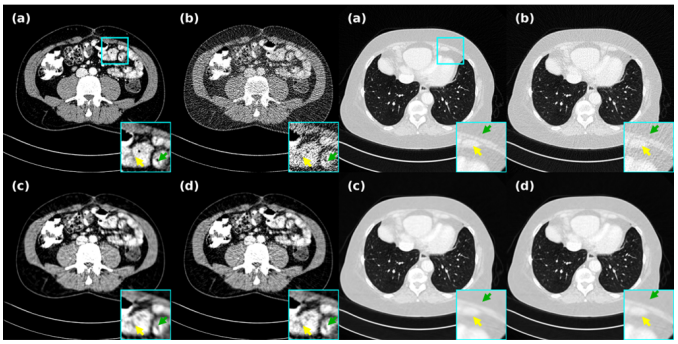

Fig. 11. Validating similarity-enhanced perceived importance ablation studies. (a) Reference (b) FBP (c) No enhance (d) Ours. The display window for abdomen images is [-100, 200] HU and for chest images is [-1350,200] HU. The blue ROIs are zoomed in for visual comparison, and the yellow and green arrows point to key details.

TABLE IV
ABLATION STUDIES (MEAN±STD) ON $\boldsymbol{\lambda}$ ON 25% DOSE TEST DATA FROM THE MAYO DATASET.

λ	PSNR ↑	SSIM(%) ↑	RMSE ↓
$\lambda = 0.5$	42.21±1.09	96.98±0.66	15.61±2.03
$\lambda = 1$	42.28±1.24	96.79±0.95	15.54±2.33
λ (Ours)	**42.41±1.21**	**96.90±2.49**	**15.30±2.21**

3) Pixel-level self-correcting validity and difference from fixed weights: The above ablation analysis for the training phase can be sufficiently justified by our approach. Subsequently, we carried out the difference between self-correction at the pixel level of the inference process and taking fixed weights. Fig. 12 and Table IV add fully illustrate the situation, with

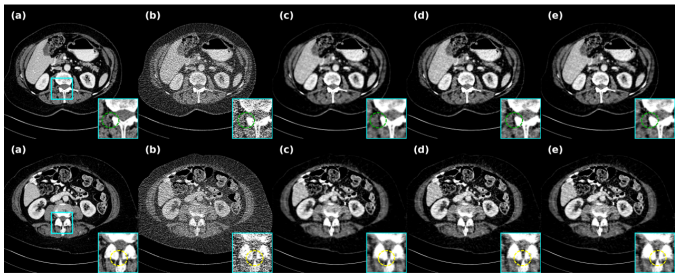

Fig. 12. Ablation studies on the effectiveness of pixel-level weighted fusion. (a) Reference (b) FBP (c) $\boldsymbol{\lambda} = \mathbf{0.5}$ (d) $\boldsymbol{\lambda} = \mathbf{1}$ (e) Ours. The display window for abdomen images is [-100, 200] HU. The blue ROIs are zoomed in for visual comparison, and the yellow and green arrows point to key details.

fixed weights we selected λ as 0.5, and even selected λ as 1, even though this is not in line with the original intent of the dual-stage. As can be seen, our pixel-level fusion can make a balance between $\hat{x}_0$ and x_{ld} for each pixel, laying the groundwork for entering into image inference, and showing competitive results in both metrics and reconstruction.

V. DISCUSSION

The purpose of the investigation in this study is to explore a distribution that requires neither paired nor clean data to solve the LDCT problem, centered on the single LDCT projection domain. This is an urgent problem that needs to be solved in current deep learning based methods as well as in clinical diagnosis. Some of the reconstruction results in this study for the lungs or abdomen still suffer from incomplete recovery of fine blood vessels and subtle blurring of localized diseased tissue, which we acknowledge is due to the fact that the noise corrupts this part of the information to a great extent, and it is not possible to model data distributions like clean data-based diffusion bases. We are planning to explore some kind of relationship similar to Wu *et al.* [44] linking between clean and noisy data to compensate for the distribution of corrupted information. Meanwhile, although our data simulation is very close to the physical model of clinical scanning, the generation of noise in real applications can be affected by factors such as patients or equipment, and the solution to this problem requires the support of huge real data. We are trying to take multiple factors into account in the reconstruction process, aiming to reach a better reconstruction result despite the absence of data labels.

VI. CONCLUSION

In this study, we proposed a novel self-supervised method, SuperDiff, for low-dose CT denoising, and it was also the first self-supervised LDCT denoising method that combines the diffusion model. The main contributions of SuperDiff were 1) proposed a self-enhancing similarity strategy for contextual sub-data, which mitigated image smoothing and provided the initial a priori as a foundation for the follow-up. 2) Combined the initial a priori with latent diffusion depth in the form of knowledge distillation. 3) The pixel-level self-correcting fusion technique in the inference process enabled the fusion of the initial a priori with the balanced LDCT image, and the

technique also provided support for generalizing the contextual sub-data. SuperDiff required only LDCT projection domain for both training and testing, and it was a self-supervised denoising method in the true sense of the word.

APPENDIX

1) Proof of Eq. (10)*:* Define $s_1(y_{ld})$, $s_2(y_{ld})$, and $s(y_0)$ as the noisy sub-data, noisy sub-target, and clean sub-data. $\varepsilon_1 = \mathbb{E}_{s_2(y_{ld})|s_1(y_0)}(s_2(y_{ld})) - s(y_0)$, $w(\varepsilon_1) = 1-\varepsilon_1$. For supervised learning:

$$\begin{aligned}&\mathbb{E}_{y_0,y_{ld}} \parallel w(\varepsilon_1) \odot (f_\theta(s_1(y_{ld})) - s(y_0)) \parallel_2^2 \\ &= \mathbb{E} \parallel w(\varepsilon_1) \odot (f_\theta(s_1(y_{ld})) - s_2(y_{ld}) + s_2(y_{ld}) - s(y_0) \parallel_2^2,\end{aligned} \tag{21}$$

under the independent condition that $s\,(y_0)$ exists, using the vector norm expansion:

$$\begin{aligned}&\mathbb{E}_{y_0,y_{ld}} \parallel w(\varepsilon_1) \odot f_\theta(s_1(y_{ld})) - s_2(y_{ld}) \parallel_2^2 \\ &= \mathbb{E}_{y_0,y_{ld}} \parallel w(\varepsilon_1) \odot f_\theta(s_1(y_{ld})) - s(y_0) \parallel_2^2 + w(\varepsilon_1)^2 \sigma^2_{s_2(y_{ld})} \\ &- 2\varepsilon_1 \mathbb{E}_{y_0,y_{ld}}(w(\varepsilon_1) \odot (f_\theta(s_1(y_{ld})) - s(y_0))),\end{aligned} \tag{22}$$

it can be seen that the relationship between the supervised $\mathbb{E}_{y_0,y_{ld}} \parallel (f_\theta(s_1(y_{ld})) - s(y_0)) \parallel_2^2$ and the self-supervised noise pair $\mathbb{E}_{y_0,y_{ld}} \parallel w(\varepsilon_1) \odot f_\theta(s_1(y_{ld})) - s_2(y_{ld}) \parallel_2^2$ contains an interaction term $2\varepsilon_1 \mathbb{E}_{y_0,y_{ld}}(\cdot)$, and ε_1 influences the optimization process. When $\varepsilon_1 \to 0$, it means the noise pairs are extremely similar, i.e., it can be equivalent to the effect of supervised loss.

However, when similarity regions exhibit excessive variation, Eq. (9) gradually widens the gap with supervised error. To address this, this study introduces $w(\varepsilon_1)$. As $\varepsilon_1 \to 1$, eliminating unreliable gap regions similarly approximates the supervised loss. ε_1 and $w(\varepsilon_1)$ function as intelligent regulators for self-enhancing similarity, achieving stable optimization and enhanced robustness. Thus, the first term of Eq. (10) is proven.

Define ε_2 as the sampling variance of the network's output results. Together with the input sampling variance ε_1, it constrains the consistency of denoising—that is, when the input variance is small, the output variance should also be small. Decoupled regularization and the first term adaptively assess variance, reduce reconstruction loss, and correct the optimization bias of output sampling.

REFERENCES

[1] D. J. Brenner and E. J. Hall, "Computed tomography—an increasing source of radiation exposure," *N. Engl. J. Med.*, vol. 357, no. 22, pp. 2277–2284, 2007.

[2] R. Smith-Bindman *et al.*, "Radiation dose associated with common computed tomography examinations and the associated lifetime attributable risk of cancer," *Arch. Intern. Med.*, vol. 169, no. 22, pp. 2078–2086, 2009.

[3] A. Sodickson *et al.*, "Recurrent CT, cumulative radiation exposure, and associated radiation-induced cancer risks from CT of adults," *Radiology*, vol. 251, no. 1, pp. 175–184, 2009.

[4] M. Balda, J. Hornegger, and B. Heismann, "Ray contribution masks for structure adaptive sinogram filtering," *IEEE Trans. Med. Imaging*, vol. 31, no. 6, pp. 1228–1239, 2012.

[5] E. Y. Sidky and X. Pan, "Image reconstruction in circular cone-beam computed tomography by constrained, total-variation minimization," *Phys. Med. Biol.*, vol. 53, no. 17, p. 4777, 2008.

[6] L. Zhu, T. Niu, and M. Petrongolo, "Iterative CT reconstruction via minimizing adaptively reweighted total variation," *J. Xray Sci. Technol.*, vol. 22, no. 2, pp. 227–240, 2014.

[7] T. E. Komolafe *et al.*, "Smoothed L0-constraint dictionary learning for low-dose x-ray CT reconstruction," *IEEE Access*, vol. 8, pp. 116,961–116,973, 2020.

[8] R. J. Geraldo, L. M. Cura, P. E. Cruvinel, and N. D. Mascarenhas, "Low dose CT filtering in the image domain using map algorithms," *IEEE Trans. Radiat. Plasma Med. Sci.*, vol. 1, no. 1, pp. 56–67, 2016.

[9] Y. Chen *et al.*, "Artifact suppressed dictionary learning for low-dose CT image processing," *IEEE Trans. Med. Imaging*, vol. 33, no. 12, pp. 2271–2292, 2014.

[10] A. Manduca *et al.*, "Projection space denoising with bilateral filtering and CT noise modeling for dose reduction in CT," *Med. Phys.*, vol. 36, no. 11, pp. 4911–4919, 2009.

[11] J. Wang, T. Li, H. Lu, and Z. Liang, "Penalized weighted least-squares approach to sinogram noise reduction and image reconstruction for low-dose x-ray computed tomography," *IEEE Trans. Med. Imaging*, vol. 25, no. 10, pp. 1272–1283, 2006.

[12] P. Perona and J. Malik, "Scale-space and edge detection using anisotropic diffusion," *IEEE Trans. Pattern Anal. Mach. Intell.*, vol. 12, no. 7, pp. 629–639, 2002.

[13] F. Catt'e, P.-L. Lions, J.-M. Morel, and T. Coll, "Image selective smoothing and edge detection by nonlinear diffusion," *SIAM J. Numer. Anal.*, vol. 29, no. 1, pp. 182–193, 1992.

[14] K. Dabov, A. Foi, V. Katkovnik, and K. Egiazarian, "Image denoising by sparse 3-D transform-domain collaborative filtering," *IEEE Trans. Image Process.*, vol. 16, no. 8, pp. 2080–2095, 2007.

[15] H. Shan *et al.*, "Competitive performance of a modularized deep neural network compared to commercial algorithms for low-dose CT image reconstruction," *Nat. Mach. Intell.*, vol. 1, no. 6, pp. 269–276, 2019.

[16] G. Wang, J. C. Ye, and B. De Man, "Deep learning for tomographic image reconstruction," *Nat. Mach. Intell.*, vol. 2, no. 12, pp. 737–748, 2020.

[17] J. Shen, M. L. Luo, H. Liu, P. Liao, H. Chen, and Y. Zhang, "Mlf-iosc: multi-level fusion network with independent operation search cell for low-dose CT denoising," *IEEE Trans. Med. Imaging*, vol. 42, no. 4, pp. 1145–1158, 2022.

[18] Q. Yang *et al.*, "Low-dose CT image denoising using a generative adversarial network with wasserstein distance and perceptual loss," *IEEE Trans. Med. Imaging*, vol. 37, no. 6, pp. 1348–1357, 2018.

[19] H. Chen *et al.*, "Low-dose CT with a residual encoder-decoder convolutional neural network," *IEEE Trans. Med. Imaging*, vol. 36, no. 12, pp. 2524–2535, 2017.

[20] Z. Huang, J. Zhang, Y. Zhang, and H. Shan, "Du-gan: Generative adversarial networks with Dual-Domain U-Net-Based Discriminators for low-dose CT denoising," *IEEE Trans. Instrum. Meas.*, vol. 71, pp. 1–12, 2022.

[21] J. Lehtinen *et al.*, "Noise2Noise: Learning image restoration without clean data," *arXiv preprint arXiv:1803.04189*, 2018.

[22] C. Niu *et al.*, "Noise suppression with similarity-based self-supervised deep learning," *IEEE Trans. Med. Imaging*, vol. 42, no. 6, pp. 1590–1602, 2022.

[23] Z. Wang, Z. Zhang, X. Zhang, H. Zheng, M. Z. Zhou, Y. Zhang, and Y. Wang, "Dr2: Diffusion-based robust degradation remover for blind face restoration," in *Proc. IEEE/CVF Conf. Comput. Vis. Pattern Recognit.*, 2023, pp. 1704–1713.

[24] J. Ho, C. Saharia, W. Chan, D. J. Fleet, M. Norouzi, and T. Salimans, "Cascaded diffusion models for high fidelity image generation," *J. Mach. Learn. Res.*, vol. 23, no. 47, pp. 1–33, 2022.

[25] T. Garber and T. Tirer, "Image restoration by denoising diffusion models with iteratively preconditioned guidance," in *Proc. IEEE/CVF Conf. Comput. Vis. Pattern Recognit.*, 2024, pp. 25,245–25,254.

[26] J. Ho, A. J. Jain, and P. Abbeel, "Denoising diffusion probabilistic models," *Adv. Neural Inf. Process. Syst.*, vol. 33, pp. 6840–6851, 2020.

[27] Y. Song, J. Sohl-Dickstein, D. P. Kingma, A. Kumar, S. Ermon, and B. Poole, "Score-based generative modeling through stochastic differential equations," *arXiv preprint arXiv:2011.13456*, 2020.

[28] E. Hoogeboom, J. Heek, and T. Salimans, "simple diffusion: End-to-end diffusion for high resolution images," in *Int. Conf. Mach. Learn.*. PMLR, 2023, pp. 13,213–13,232.

[29] C. Lu, Y. Zhou, F. Bao, J. Chen, C. Li, and J. Zhu, "Dpm-solver: A fast ode solver for diffusion probabilistic model sampling in around 10 steps," *Adv. Neural Inf. Process. Syst.*, vol. 35, pp. 5775–5787, 2022.

[30] K. Zheng, C. Lu, J. Chen, and J. Zhu, "Dpm-solver-v3: Improved diffusion ode solver with empirical model statistics," *Adv. Neural Inf. Process. Syst.*, vol. 36, pp. 55,502–55,542, 2023.

[31] F. Liao, Y. Tang, Q. Du, J. Wang, M. Li, and J. Zheng, "Domain progressive low-dose CT Imaging using Iterative Partial Diffusion Model," *IEEE Trans. Med. Imaging*, 2024.

[32] R. Rombach, A. Blattmann, D. Lorenz, P. Esser, and B. Ommer, "High-resolution image synthesis with latent diffusion models," in *Proc. IEEE/CVF Conf. Comput. Vis. Pattern Recognit.*, 2022, pp. 10,684–10,695.

[33] H. Nam, G. Kwon, G. Y. Park, and J. C. Ye, "Contrastive denoising score for text-guided latent diffusion image editing," in *Proc. IEEE/CVF Conf. Comput. Vis. Pattern Recognit.*, 2024, pp. 9192–9201.

[34] C. Meng *et al.*, "On distillation of guided diffusion models," in *Proc. IEEE/CVF Conf. Comput. Vis. Pattern Recognit.*, 2023, pp. 14,297–14,306.

[35] V. T. Hu, D. W. Zhang, Y. M. Asano, G. J. Burghouts, and C. G. Snoek, "Self-guided diffusion models," in *Proc. IEEE/CVF Conf. Comput. Vis. Pattern Recognit.*, 2023, pp. 18,413–18,422.

[36] J. Batson and L. Royer, "Noise2self: Blind denoising by self-supervision," in *Int. Conf. Mach. Learn.*. PMLR, 2019, pp. 524–533.

[37] A. Krull, T.-O. Buchholz, and F. Jug, "Noise2void-learning denoising from single noisy images," in *Proc. IEEE/CVF Conf. Comput. Vis. Pattern Recognit.*, 2019, pp. 2129–2137.

[38] Y. Xie, Z. Wang, and S. Ji, "Noise2same: Optimizing a self-supervised bound for image denoising," *Adv. Neural Inf. Process. Syst.*, vol. 33, pp. 20,320–20,330, 2020.

[39] N. Moran, D. Schmidt, Y. Zhong, and P. Coady, "Noisier2noise: Learning to denoise from unpaired noisy data," in *Proc. IEEE/CVF Conf. Comput. Vis. Pattern Recognit.*, 2020, pp. 12,064–12,072.

[40] T. Huang, S. Li, X. Jia, H. Lu, and J. Liu, "Neighbor2neighbor: Self-supervised denoising from single noisy images," in *Proc. IEEE/CVF Conf. Comput. Vis. Pattern Recognit.*, 2021, pp. 14,781–14,790.

[41] T. Huang, S. Li, X. Jia, H. Lu and Z. Liu "Neighbor2neighbor: A self-supervised framework for deep image denoising," *IEEE Trans. Image Process.*, vol. 31, pp. 4023–4038, 2022.

[42] T. Pang, H. Zheng, Y. Quan, and H. Ji, "Recorrupted-to-recorrupted: Unsupervised deep learning for image denoising," in *Proc. IEEE/CVF Conf. Comput. Vis. Pattern Recognit.*, 2021, pp. 2043–2052.

[43] Y. Wang *et al.*, "SVB: Self-Supervised Real CT Denoising via Similarity-Based Visual Blind-Spot Scheme," *IEEE Trans. Instrum. Meas.*, 2024.

[44] Q. Wu *et al.*, "Unsharp structure guided filtering for self-supervised low-dose CT imaging," *IEEE Trans. Med. Imaging*, vol. 42, no. 11, pp. 3283–3294, 2023.

[45] M. O. Unal, M. Ertas, and I. Yildirim, "Proj2Proj: self-supervised low-dose CT reconstruction," *PeerJ Comput. Sci.*, vol. 10, p. e1849, 2024.

[46] Q. Gao, Z. Li, J. Zhang, Y. Zhang, and H. Shan, "Corediff: Contextual error-modulated generalized diffusion model for low-dose CT denoising and generalization," *IEEE Trans. Med. Imaging*, vol. 43, no. 2, pp. 745–759, 2023.

[47] Q. Gao, Z. Chen, D. Z. Zeng, J. Zhang, J. Ma, and H. Shan, "Noise-Inspired Diffusion Nodel for Generalizable low-dose CT Reconstruction," *arXiv preprint arXiv:2506.22012*, 2025.

[48] B. Yang, Z. Jiang, D. Pan, H. Yu, G. Gui, and W. Gui, "LFDT-Fusion: A latent feature-guided diffusion Transformer model for general image fusion," *Inf. Fusion*, vol. 113, p. 102639, 2025.

[49] H. Li, W. Zhang, X. Hu, T. Jiang, Z. Chen, and H. Wang, "Prompt-SID: Learning Structural Representation Prompt via Latent Diffusion for Single Image Denoising," in *Proc. AAAI Conf. Artif. Intell.*, vol. 39, no. 5, 2025, pp. 4734–4742.

[50] M. Zhussip, S. Soltanayev, and S. Y. Chun, "Extending stein's unbiased risk estimator to train deep denoisers with correlated pairs of noisy images," *Adv. Neural Inf. Process. Syst.*, vol. 32, 2019.

[51] T. R. Moen *et al.*, "Low-dose CT image and projection dataset," *Med. Phys.*, vol. 48, no. 2, pp. 902–911, 2021.

[52] D. Zeng *et al.*, "A simple low-dose x-ray CT simulation from high-dose scan," *IEEE Trans. Nucl. Sci.*, vol. 62, no. 5, pp. 2226–2233, 2025.

[53] S. G. Armato III *et al.*, "The lung image database consortium (LIDC) and image database resource initiative (IDRI): a completed reference database of lung nodules on CT scans," *Med. Phys.*, vol. 38, no. 2, pp. 915–931, 2011.

[54] S. Laine, T. Karras, J. Lehtinen, and T. Aila, "High-quality self-supervised deep image denoising," *Adv. Neural Inf. Process. Syst.*, vol. 32, 2019.

[55] L. I. Rudin, S. Osher, and E. Fatemi, "Nonlinear total variation based noise removal algorithms," *Physica D*, vol. 60, no. 1-4, pp. 259–268, 1992.

[56] Z. Wang, J. Liu, G. Li, and H. Han, "Blind2unblind: Self-supervised image denoising with visible blind spots," in *Proc. IEEE/CVF Conf. Comput. Vis. Pattern Recognit.*, 2022, pp. 2027–2036.

[57] H. Liu, J. Fu, Q. Xie, and D. Meng, "Rotation-Equivariant Self-Supervised Method in Image Denoising," in *Proc. IEEE/CVF Conf. Comput. Vis. Pattern Recognit.*, 2025, pp. 12,720–12,730.

[58] Z. Wang, A. C. Bovik, H. R. Sheikh, and E. P. Simoncelli, "Image quality assessment: from error visibility to structural similarity," *IEEE Trans. Image Process.*, vol. 13, no. 4, pp. 600–612, 2004.

[59] L. Zhang, L. Zhang, X. Mou, and D. Zhang, "FSIM: A feature similarity index for image quality assessment," *IEEE Trans. Image Process.*, vol. 20, no. 8, pp. 2378–2386, 2011.

[60] H. R. Sheikh and A. C. Bovik, "Image information and visual quality," *IEEE Trans. Image Process.*, vol. 15, no. 2, pp. 430–444, 2006.

[61] N. Damera-Venkata, T. D. Kite, W. S. Geisler, B. L. Evans, and A. C. Bovik, "Image quality assessment based on a degradation model," *IEEE Trans. Image Process.*, vol. 9, no. 4, pp. 636–650, 2000.